Surface Urban Heat Island (S-UHI) investigations using remote sensing

Report

Author(s):
Philipp, Conrad H.

Publication date:
2019-10-23

Permanent link:
https://doi.org/10.3929/ethz-b-000372356

Rights / license:
In Copyright - Non-Commercial Use Permitted

Originally published in:
Deliverable Technical Report

DELIVERABLE
TECHNICAL REPORT
Version 23/20/2019

D1.2a – Surface Urban Heat Island (S-UHI) investigations using remote sensing.

Project ID	NRF2019VSG-UCD-001
Project Title	Cooling Singapore 1.5: Virtual Singapore Urban Climate Design
Deliverable ID	D1.2a - Surface Urban Heat Island (S-UHI) investigations using remote sensing.
Authors	Conrad Philipp
Contributors	Omer Mughal (data support), Sailin Zhong (visualization of several data sets in Singapore Views)
Date of Report	23/10/2019

Version	Date	Modifications	Reviewed by
1	13/08/2019	Original	Leslie Norford, Winston Chow

1 Abstract

Roth (2013:145) defines and differentiates urban heat island (UHI) phenomena associated with air and surface temperatures: "The Canopy-Layer UHI (CL-UHI) and the Urban-Boundary Layer UHI (UBL-UHI) refer to a warming of the urban atmosphere whereas the Surface UHI (S-UHI) refers to a warming of the surface. The S-UHI … is a surface energy balance phenomenon and involves all urban facets (street, roofs, trees, etc.). Urban surface temperatures are sensitive to the relative orientation of the surface components to the sun by day and the sky at night, as well as to their thermal (e.g., heat capacity, thermal admittance) and radiative (e.g., reflectivity or albedo) properties. It is strongest during daytime when solar heating creates large differences between dry/wet and vegetated surfaces, horizontal surfaces such as roofs and pavements (industrial-commercial zones, especially those with large, flat-topped buildings or extensive open areas of pavement e.g., airport, shopping malls, and major highway intersections). At night, some of the processes are reduced, and urban-rural differences and intra-urban variability of surface temperature are smaller than during the day". Within this study meso-scale Urban Heat Island (UHI) assessment through remote sensing will be carried out to support the following essential urban climate research tasks: • Calculation of the surface temperature for Singapore via satellite based remote sensing data to map temporal changes of the Surface UHI (S-UHI) over the last decades. • Provision of environmental input data, products and information that shape the exposure to urban heat such as land cover, street geometry, building volume, large floor area, aspect ratio, shading, land use and land surface to be directly integrated into climate models (e.g. Cosmo, WRF). • Providing data that help to support the validation of the meso-scale canopy-layer models (e.g. SingV, WRF). • Processed output data to be incorperated into Singapore Views for visualization purposes.

Table of Content

2 Introduction

2.1 Objectives

The meso-scale Urban Heat Island (UHI) assessment through remote sensing will be carried out to support the following essential urban climate research tasks:

- **Calculation** of the surface temperature for Singapore via satellite based remote sensing data to map temporal changes of the Surface UHI (S-UHI) over the last decades.
- Provision of environmental **input data**, products and information that shape the exposure to urban heat such as land cover, street geometry, building volume, large floor area, aspect ratio, shading, land use and land surface to be directly integrated into climate models (e.g. SingV, WRF).
- Providing data that help to support the **validation** of the meso-scale canopy-layer models (e.g. SingV, WRF).
- Processed output data to be incorporated into Singapore Views for **visualization** purposes.

2.2 Hypothesis

The aim of this task is to achieve the following goals:

- Remote sensing allow investigating the surface temperature for Singapore via satellite based remote sensing data (Landsat-5 and -8) to map Singapore's Surface Urban Heat Island (S-UHI) under the challenging circumstance of frequent cloud coverage.
- Remote sensing data will support the investigation of temporal changes of S-UHI through to satellite day-time images of land cover modifications of the last decades.
- Remote sensing data will allow to compare the Land Surface Temperature (LST) vs Local Climate Zones (LCZ) day-timenight-timefor day- and night-time.
- Remote sensing investigations will enable to locate the surface temperature of the hottest and coldest districts (based on LST) for day- and night-time. day-timenight-time
- Remote sensing investigations will enable to locate the surface temperature of hot spots and cold spots in relation to LCZ for day- and night-time. day-timenight-time
- Remote sensing will provide environmental input data, products and information that shape the exposure to urban heat such as land cover, street geometry, building volume, large floor area, aspect ratio, shading, land use and land surface to be directly integrated into climate models (e.g. SingV, WRF).
- Remote sensing data will support the validation of the meso-scale canopy-layer models (e.g. SingV, WRF).
- Related remote sensing data will allow the comparison of surface-UHI and air temperature-UHI (initially for CS1.5 and in-depth under CS2.0).
- Remote sensing data will support the guidance on urban planning / urban geometry to mitigate UHI and optimize outdoor thermal comfort (OTC).
- Remote sensing data will support the development of a vulnerability map (see D2.3c) and other task of CS1.5.
- Primary investigations of Singapore's S-UHI via remote sensing will promote the related research for further investigations in Singapore and the tropics.

3 Methods

3.1 Preparation

- Data from the free-of-charge, accessible remote sensing satellite project Landsat were organized (Earthexplorer 2019).
- Cloud-free Landsat images were used for Land Surface Temperature (LST) calculations, including data from Landsat-5 Thematic Mapper (TM) obtained on 13 September 1989 and 25 December 2003, and Landsat8 Thermal Infrared Sensor (TIRS) data obtained on 11 October 2015 and 24 May 2018.
- Post-processed data from twelve Landsat-8 imageries were used to receive a Local Climate Zones (LCZ) map (Mughal et al., 2019).

3.2 Design of the experiment / modelling

- Urban heat Island studies support the concept that the land cover surfaces affect the heat balance in the built environment, and the magnitude of Surface UHI (S-UHI) effect varies across scales and different land surface materials. The types of materials (which affect their thermal properties) and their area of coverage (which affects heat accumulation) can significantly alter the S-UHI effect.
- The LST calculation workflow is illustrated in Fig. 1 and described as follow:
    - First step: land cover classification (see 2.3.1).
    - Second step: atmospheric correction (see 2.3.2)
- The software eCognition, ArcGIS 10.0 and Quantum GIS 3.8 were used to undertake the related raster calculations
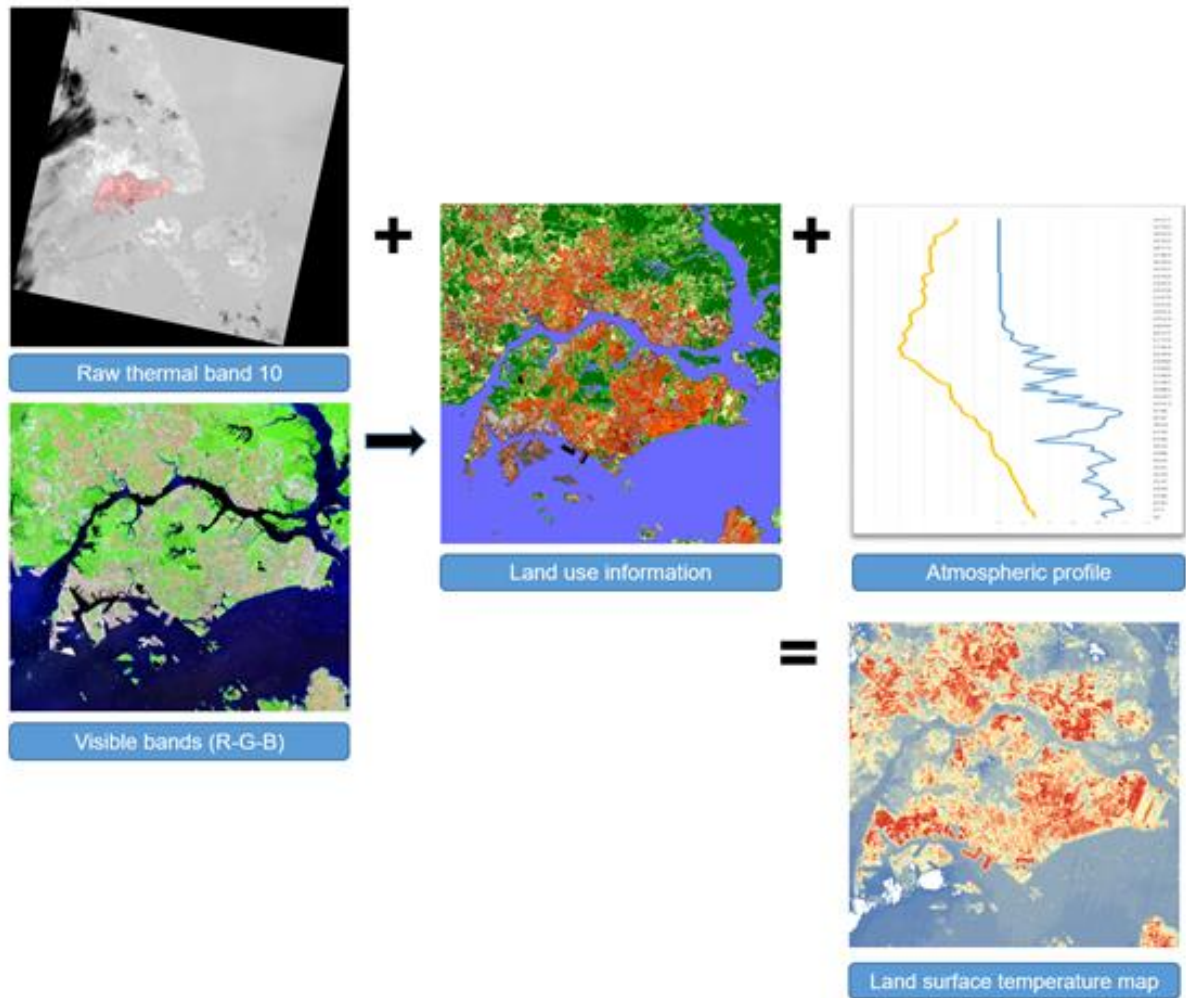
Figure 1. The workflow of the land surface temperature map calculation based on Landsat satellite imageries: The surface temperature maps are created based on a land use information classification by means of the Landsat R-G-B visible bands (see 2.3.1) , as well as, on an atmospheric correction of the raw thermal band of Landsat (Source: Wyoming 2019, Mughal et al., 2019 and Earthexplorer 2019) using the atmospheric temperature and humidity profiles (see 2.3.2).

3.3 Experiment

Local climate zone (LCZ) classification

The Local Climate Zone (LCZ) map for Singapore (Fig. 2) was developed by Mughal et al., 2019 following the WUDAPT methodology (Ching et al., 2018) for level 0 data (Mills et al., 2015) using Landsat-8 imageries and high-resolution building height data.
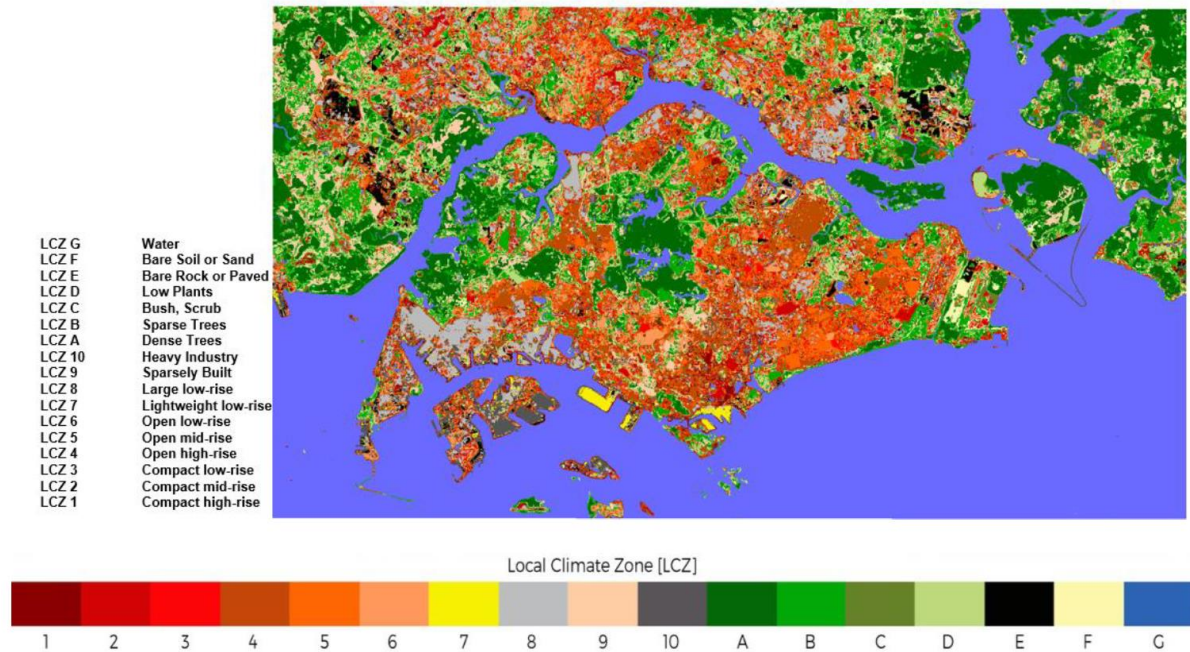

LCZ G	Water
LCZ F	Bare Soil or Sand
LCZ E	Bare Rock or Paved
LCZ D	Low Plants
LCZ C	Bush, Scrub
LCZ B	Sparse Trees
LCZ A	Dense Trees
LCZ 10	Heavy Industry
LCZ 9	Sparsely Built
LCZ 8	Large low-rise
LCZ 7	Lightweight low-rise
LCZ 6	Open low-rise
LCZ 5	Open mid-rise
LCZ 4	Open high-rise
LCZ 3	Compact low-rise
LCZ 2	Compact mid-rise
LCZ 1	Compact high-rise

Local Climate Zone [LCZ]

1 2 3 4 5 6 7 8 9 10 A B C D E F G

Figure 2. Map of LCZs over Singapore using the Random Forest Classification (Mughal et al., 2019).

Twelve Landsat-8 images (level 1 images of 2015-2017) with a resolution of 30 m and a cloud cover less than 20% were seamlessly mosaicked to account for the high cloud coverage over Southeast Asia and Singapore. The Fmask algorithm (Qiu et al., 2017, Zhu, Wang and Woodcock, 2015) was applied before to further separate cloud cirrus, shadow and water from clear pixels. This image, together with data for building height and vegetation were used for the SAGA GIS software (Conrad et al., 2015) to discriminate between spectral attribute and building height of different LCZ types based on the training areas, which were created by digitizing parts of the city and the surrounding areas that represent exemplars of LCZ types in the study area based on researchers' local knowledge (Mughal et al., 2019).

The pixels in the study area were automatically classified into the LCZ types (Bechtel and Daneke, 2012, Bechtel et al., 2015) by SAGA GIS using the digitized areas. The training areas were refined and new ones were added iteratively until the outcome was satisfactory. To perform an accuracy assessment, a total of 415 validation points was randomly selected based on the classified LCZ map to compare with Google Earth imagery at each validation point. The calculated overall accuracy based on the confusion matrix C (Wang et al., 2018, Middel et al., 2018), is 70% in the urban areas (which means reliable according to Bechtel et

al., 2019). The final map should be treated as a general rather than a precise description of the city and its surrounding environment.

The urbanized landscape covers 420 km² (Angel et al., 2016), the majority of which is as per Mughal et al., 2019:

Open High Rise   (LCZ4, 25.1 %), while the rest includes
Compact High Rise   (LCZ1, 3.3 %),
Compact Mid Rise   (LCZ2, 9.7 %),
Compact Low Rise   (LCZ3, 3.0 %),
Open Mid Rise   (LCZ5, 18.3 %),
Open Low Rise   (LCZ6, 8.7 %),
Light Weight Low Rise (LCZ7, 2.0 %),
Large Low Rise   (LCZ8, 12.4 %),
Sparsely Built   (LCZ9, 9.9 %) and
Heavy Industry   (LCZ10, 7.0 %).

Modified Mono-Window Algorithm

Remote sensing imageries consist of matrices of digital numbers DN to represent each pixel of the land surface. For the thermal bands of the satellites, the individual values of spectral radiance at the sensor's aperture, L, can be estimated:

$$L = G_{rescale} \times DN + B_{rescale}, \tag{1}$$

where the pairs of the actual calibration parameters $G_{rescale}$ and $B_{rescale}$ follow Table 1 (Barsi, 2014), however, Band 11 of Landsat-8 is not listed due to its unsolved calibration problems.

Table 1. Thermal band characteristics and parameters for Landsat satellites.

Satellite	Instrument	Band	from	to	$G_{rescale}$ in W/m²sr μm	$B_{rescale}$ in W/m²sr μm
Landsat-5	TM	6 (NLAPS)	March 1984	April 2007	0.055158	1.2378
		6 (LPGS)	April 2007	June 2013	0.055374	1.1826
Landsat-7	ETM+	61 (Low gain)	April 1999	present	0.067087	-0.0671
		62 (High gain)	April 1999	present	0.037205	3.1628
Landsat-8	TIRS	10	May 2013	present	0.0003342	0.1

To connect this spectral radiance with the temperature of the pixel, Planck's law is used to describe the relation between the temperature T and the emitted radiation of wavelength λ in case of black bodies:

$$B(T, \lambda) = 2\,h\,c^2\,\lambda^{-5} / [\exp(h\,c\,/\,k\,\lambda\,T) - 1], \tag{2}$$

using three universal parameters (Table 2).

Table 2. Natural constants in Planck's law.

Parameter	Name	value
h	Planck's constant	6.6260696E-34 W s²
c	Vacuum light speed	2.9979246E+8 m / s
k	Boltzmann's constant	1.3806488E-23 W s / K

Their combination creates:

$$B(T, \lambda) = C_1\,\lambda^{-5} / [\exp(C_2\,/\,\lambda\,T) - 1] \tag{3}$$

with two formal values (Table 3).

Table 3. Formal constants in Planck's law.

Parameter	origin	value
C_1	$= 2\,h\,c^2$	1.1910436E+8 W µm⁴ / m² sr
C_2	$= h\,c^2\,/\,k$	1.4387685E+4 µm K

If only one individual wavelength is considered, the inversion of Equation (3) is possible:

$$T = C_2 / [\lambda \times \ln(1 + C_1\,\lambda^{-5}\,B^{-1})]. \tag{4}$$

However, in case of remote sensing the emitted radiation is combined over the measuring range of wavelengths from λ_{min} to λ_{max}. Due to the technical characteristics of each instrument, this compacting does not occur uniformly, but as per relative spectral response functions RSR (Fig. 3).
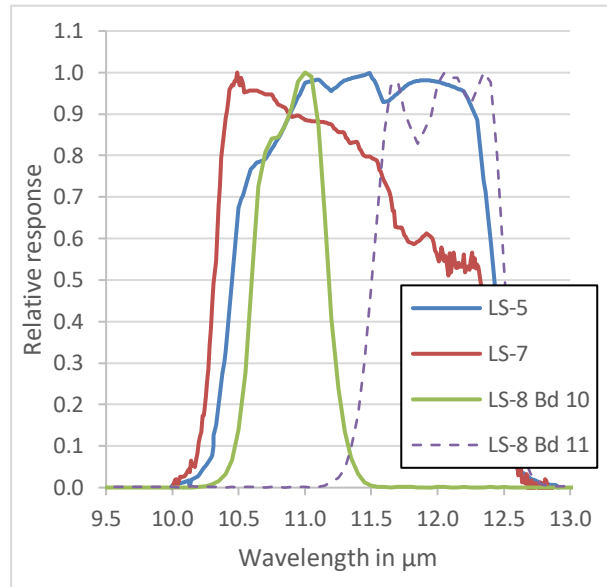

Figure 3. Relative spectral response of the thermal bands of the Landsat satellites.

The measured channel-integrated radiance L at a temperature T is defined as a weighted mean:

$$L\,(T) = \frac{\int_{\lambda min}^{\lambda max} B\,(T,\lambda) \times RSR\,(\lambda)\,d\lambda}{\int_{\lambda min}^{\lambda max} RSR\,(\lambda)\,d\lambda} \tag{5}$$

and can be estimated by numerical integration of both the numerator and the denominator.

As the terrestrial ground temperatures of areas to be investigated are most likely to be between -30 °C and 70 °C (i. e. 243.15 K .. 343.15 K), the calculation according to Equation (5) was done for every instrument in steps of 5 K of this interval. The aim of this new method was to express a continuous relation of power series type:

$$L\,(T) = \sum_{k=0}^{n} \left(a_k \times T^k \right), \tag{6}$$

and the multiple linear regression showed, that fourth order approximations:

$$L\,(T) = a_4 \times T^4 + a_3 \times T^3 + a_2 \times T^2 + a_1 \times T + a_0 \tag{7}$$

exclusively contain significant non-zero coefficients (Tab. 4) and thus they are sufficient to give a best possible fitting for L(T) (Tab. 5). The drawback of missing physical interpretability of the coefficients has been predominated by the advantage of highest accuracy and flexibility to any set of original data.

Table 4. Regression coefficients for Equation (7).

Satellite	Inst.	a_4 in W/m²sr μm K^4	a_3 in W/m²sr μm K^3	a_2 in W/m²sr μm K^2	a_1 in W/m²sr μm K	a_0 in W/m²sr μm
Landsat-5	TM	-2.12473E-9	2.41587E-6	-5.10549E-4	1.56262E-2	2.52713
Landsat-7	ETM+	-2.35511E-9	2.73424E-6	-6.40411E-4	3.64885E-2	1.34227
Landsat-8	TIR-1	-2.70967E-9	3.21260E-6	-8.29557E-4	6.57793E-2	-0.25181

Table 5. Determination coefficients R² and standard errors S for regression coefficients of Table 4.

Satellite	Inst.	R^2	S
Landsat-5	TM	1.00000000	9.631248E-5
Landsat-7	ETM+	1.00000000	9.901541E-5
Landsat-8	TIR-1	1.00000000	1.052240E-4
	TIR-2	1.00000000	8.723299E-5

In an analogous way the inversion of Equation (6) can be done:

$$T\,(L) \;=\; \sum_{k=0}^{n}\left(b_k \times L^k\right), \tag{8}$$

while for the same data triples (λ; T; L) a seventh order power series:

$$T = b_7 \times L^7 + b_6 \times L^6 + b_5 \times L^5 + b_4 \times L^4 + b_3 \times L^3 + b_2 \times L^2 + b_1 \times L + b_0 \tag{9}$$

should be applied (Tabs. 6 and 7), instead of simple linearized Taylor expansion (Qin et al. 2016, Wang et al., 2003).

Table 6. Regression coefficients for Equation (9).

Sat.	Inst.	b_7 in K × (W/m²sr μm)$^{-7}$	b_6 in K × (W/m²sr μm)$^{-6}$	b_5 in K × (W/m²sr μm)$^{-5}$	b_4 in K × (W/m²sr μm)$^{-4}$
LS-5	TM	1.075760E-6	-8.349834E-5	2.775651E-3	-5.184806E-2
LS-7	ETM+	9.809692E-7	-7.738280E-5	2.612019E-3	-4.949187E-2
LS-8	TIR-1	8.292848E-7	-6.725621E-5	2.330953E-3	-4.527711E-2

Sat.	Inst.	b_3 in K × (W/m²sr μm)$^{-3}$	b_2 in K × (W/m²sr μm)$^{-2}$	b_1 in K ×(W/m²sr μm)$^{-1}$	b_0 in K
LS-5	TM	6.033896E-1	-4.681567	3.105939E1	1.731415E2
LS-7	ETM+	5.834999E-1	-4.579206	3.055998E1	1.744445E2
LS-8	TIR-1	5.462043E-1	-4.375876	2.961365E1	1.765610E2

Table 7. Determination coefficients R² and standard errors S for regression coefficients of Tab. 6.

Satellite	Inst.	R^2	S
Landsat-5	TM	1.00000000	4.459165E-4
Landsat-7	ETM+	1.00000000	1.608649E-3
Landsat-8	TIR-1	1.00000000	1.933453E-3

With the L-values derived from a remote sensing picture according to Equation (1) the brightness temperatures T_b can be computed using Equation (9). They are determined by the radiation that arrives at the satellites, i. e. as though emitted by a fictitious blackbody that would be located directly in front of the instruments.

Correction from Brightness Temperatures to Land Surface Temperatures

During its penetration through the atmosphere the emitted radiance is weakened by absorption, but also amplified by atmospheric emittances. The latter can be split into an up-dwelling portion L_{up} that reaches the probe directly and into a down-dwelling share L_{down} that will be reflected by the ground and, therefore, also reduced by atmospheric absorption. Furthermore, each investigated pixel area of the earth's surface is considered to be non-black and LAMBERTian, i. e. the uniform radiation to every direction can be expressed as product of

blackbody radiation L (T_s) and ground emissivity ε, while (1-ε) defines the share of reflecting (i. e. non-absorbing) a radiation that has arrived at the surface.

The mentioned balance, called Radiation Transfer Equation (RTE), forms a reference to the brightness temperature T_b:

$$L\ (T_b) = ε × τ × L\ (T_s) + (1 − ε) × τ × L_{down} + L_{up}. \tag{10}$$

Qin et al., 2001 developed the Mono-Window Algorithm (MWA) to handle the atmospheric correction and postulated the strong similarity of the two components of atmospheric emittance at a fictitious temperature T_a:

$$L_{down} ≈ L_{up} = (1 − τ) × L\ (T_a), \tag{11}$$

to be approximated according to Sobrino et al., 1990 as effective mean atmospheric temperature by:

$$T_a = \frac{\int_0^A T(z) × w(z)\ dz}{W}, \tag{12}$$

with the altitude A of the satellite, the vertical temperature profile T(z) from nadir to probe, and the vertical water content w(z) of the atmosphere on the same path. Furthermore, the total atmospheric water content W from nadir to the altitude of the instruments is defined as:

$$W = \int_0^A w(z)\ dz. \tag{13}$$

Normally, the height profile of the absolute water content w(z) is not accessible, but the relative humidity RH(z) is, and only multiplying by the local atmospheric saturation humidity SH(z) must be done:

$$w(z) = RH\ (z) × SH\ (z). \tag{14}$$

This saturation value that depends only on the local temperature T(z) in K, or $\vartheta(z)$ in °C, can be extracted from physical tables (e. g. [..]) and is fitted best (see Table 8) by an exponential fifth degree power series:

$$SH\ (z) = SH\ (\vartheta(z)) = \exp\left[\sum_{k=0}^5 (d_k × \vartheta(z)^k)\right]\ g/m³, \tag{15}$$

with coefficients according to Tab. 9.

Table 8. Determination coefficient R^2 and standard error S for regression coefficients of Tab. 9.

R²	S
1.00000000	7.911849E-5

Table 9. Regression coefficients for Equation (15).

d_5	d_4	d_3	d_2	d_1	d_0
in (°C)$^{-5}$	in (°C)$^{-4}$	in (°C)$^{-3}$	in (°C)$^{-2}$	in (°C)$^{-1}$	in 1
2.0344E-11	-4.28431E-9	1.10288E-6	-2.91730E-4	6.89899E-2	1.57861

In the multitude of studies dealing with urban agglomerations there is an access to weather stations, where meteorological balloons are launched to provide atmospheric profiles of temperature and relative humidity close to the areas under remote sensing investigation. Typically, the profiles are measured several times a day, allowing an interpolation for the satellite overpass time t_{OP}:

$$T(t_{OP}) = \frac{T_1 \, x \, f(t_2) - T_2 \, x \, f(t_1) + (T_2 - T_1) \, x \, f(t_{OP})}{f(t_2) - f(t_1)} \, , \tag{16}$$

on the basis of:

$$f(t) = \cos^2(\pi \frac{t - t_{max}}{24}) \, , \tag{17}$$

with the times of measurement t_1 and t_2 (in h) and their assigned temperatures T_1 and T_2, as well as, t_{max} (in h) as time of the maximum temperature taken from this day's meteorological records.

The mean atmospheric temperature T_a is estimated by numerical integration as per Equations (12) and (13), and there is no need to use any linear approximation of the relation between this T_a and the near surface temperature T_o, as suggested in Qin et al., 2001.

From Equation (10) with (11) and (12) follows:

$$L(T_s) = L(T_b) / C - D / C \times L(T_a) \tag{18}$$

with

$$C = \varepsilon \times \tau \tag{19}$$

and

$$D = [1 + (1 - \varepsilon) \times \tau] \times (1 - \tau), \tag{20}$$

as the basic relation to enable an inversion to the land surface temperature (LST) T_s according to Equation (9), while the value of L (T_b) is taken from the spectral radiance L according to Equation (1).

2.3.2.3 Estimation of the atmospheric transmittance τ

During its penetration through the atmosphere the emitted radiance is weakened by absorption, and in the thermal bands almost solely the water molecules are responsible for it. Wang et al., 2003 presented for Landsat-8 a variety of stepwise linear approximations how the transmittance τ depends on the total atmospheric water content W under different regional and seasonal conditions. However, in this study τ was referred to W and the nadir air temperature T_o to provide a general cubic power series of these two variables:

$$\tau = c_9 \times T_0{}^2 \times W + c_8 \times T_0 \times W^2 + c_7 \times T_0{}^3 + c_6 \times T_0{}^2 + c_5 \times T_0 \times W + c_4 \times T_0 + c_3 \times W^3 + c_2 \times W^2 + c_1 \times W + c_0. \quad (21)$$

Due to several demands on LST-evaluations from Egypt to Australia and Japan, ten cities were taken as reference locations (Tab. 10). They cover a wide and typical area of climates, as their KÖPPEN-GEIGER classification (see Peel et al., 2007) demonstrates. The data basis to execute the regression was formed by 24 sets for every city, i. e. at 0, 6, 12, and 18 o'clock GMT of January, March, May, July, September, as well as, November, 2014. Actual atmospheric measurements (Wyoming 2019) were used to obtain the height profiles of temperature and relative humidity. Since their outputs also contain the atmospheric transmission values for each of the Landsat types, it was only necessary to calculate W according to Equations (13) to (15).

Table 10. Cities involved in τ -regression.

City	Coordinates		Climate	analogous	Köppen-Geiger classification
Harbin	45° 45' N	126° 38' E	monsoon-influenced, humid continental	Beijing	Dwa
Seoul	37° 34' N	126° 59' E	humid continental / subtropical transitional		Dwa/Cwa
Xian	34° 16' N	108° 54' E	semi-arid / humid continental	Tehran	BSk/Cwa
Cairo	30° 03' N	31° 14' E	hot desert		BWh
Hong Kong	22° 18' N	114° 10' E	monsoon-influenced, humid subtropical		Cwa
Mumbai	18° 59' N	72° 50' E	tropical wet and dry	Dacca	Aw
Singapore	1° 17' N	103° 50' E	tropical rainforest		Af
Sydney	33° 52' S	151° 13' E	humid subtropical	Tokyo, Taipei	Cfa
Adelaide	34° 56' S	138° 36' E	hot-summer Mediterranean		Csa
Melbourne	37° 49' S	144° 58' E	oceanic	Nairobi	Cfb

For each Landsat instrument, the regression was started with the full approach (21), but stepwise the regression coefficients without significance were removed until final and sufficient terms remained in form of Equation (22) with coefficients according to Tab. 11:

$$T = c_5 \times T_0 \times w + c_4 \times T_0 + c_3 \times w^3 + c_2 \times w^2 + c_1 \times w + c_0. \tag{22}$$

Only for Landsat-5 the mixed term $T_0 \times w$ is clearly non-zero, while in case of the other two thermal bands c_5 falls out. The statistical criteria of the regressions (Tab. 12) indicate an excellent fit for the entire geographical scope of involved cities by day and by night, as well as, in summer and in winter, and no subjective selection of the respective standard atmosphere situation is necessary.

Table 11. Regression coefficients for Equation (22).

Sat. Inst.	c_5 in (cm²/g K)	c_4 in K⁻¹	c_3 in (cm²/g)³	c_2 in (cm²/g)²	c_1 in cm²/g	c_0 in 1
LS-5 TM	3.74513E-4	-8.58991E-4	1.98170E-3	-1.39470E-2	-1.12740E-1	1.00993
LS-7 ETM+	0	-9.93776E-4	2.13300E-3	-1.59891E-2	-9.19105E-2	1.00295
LS-8 TIR-1	0	-3.01473E-4	2.03381E-3	-1.72079E-2	-7.45679E-2	1.00452

Table 12. Determination coefficient R² and standard error S for regression coefficients of Table 11.

Satellite	Inst.	R²	S
Landsat-5	TM	0.99289	0.0189
Landsat-7	ETM+	0.99449	0.0167
Landsat-8	TIR-1	0.99360	0.0163

Specification of the ground emissivity ε

Due to the limited availability of historical land-use information and time constrains of this pilot study, the specification of ε was omitted, and all pixel values were assigned with 0.9. Further investigation will specify ε-values for each LCZ within a typical range from 0.9 for urban areas to 0.99 for water, based on a specifically developed LCZ map following the procedure within chapter 2.3.1 for April 2016 [Mughal et al, 2019].

4 Results

4.1 Outputs

The following outputs of this investigation of land surface temperatures via remote sensing data from the satellite Landsat 5-8 could be generated:

- Land surface temperature maps for Singapore: 13 September 1989 (10:42 am), 25 December 2003 (10.55am), 11 October 2015 (11.14pm) and 24 May 2018 (11.15am).
- Detection and mapping of Singapore's land surface temperatures in relation to the Local Climate Zones (LCZ) for 24 May 2018 (11.15am) and 11 October 2015 (11.14pm).
- Detection and mapping of Singapore's hottest and coldest land surface temperatures in relation to districts (Total: 55) and subzones (Total: 323) for 24 May 2018 (11.15am) and 11 October 2015 (11.14pm).
- Environmental input data, products and information that shape the exposure to urban heat such as land cover, street geometry, building volume, large floor area, aspect ratio, shading, land use and land surface to be directly integrated into climate models (e.g. SingV, WRF)
- Data that help to support the validation of the meso-scale canopy-layer models (e.g. SingV, WRF)
- Post-processed data for the visualization in Singapore Views

4.2 Analysis

The analysis led to the following findings:

- A remote sensing day-time image of 24 May 2018 (11.15am, see Fig. 4) and a remote sensing night image of 11 October 2015 (11.14pm) were used to distinguish the average surface temperature of different land cover types and Local Climate Zones for Singapore.
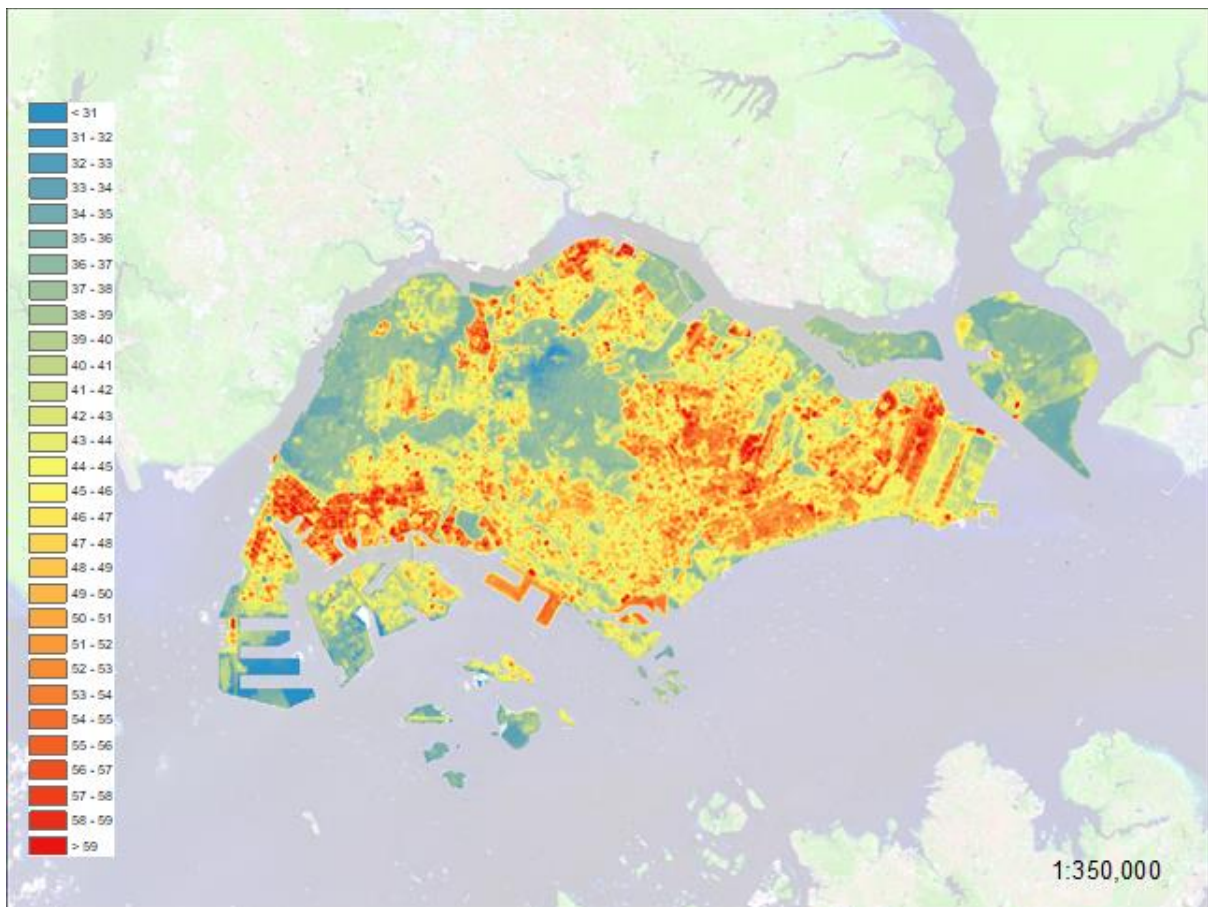
Figure 4. Surface temperatures in °C for 24 May 2018 (11.15 am local time) (Source: Earthexplorer 2019).

- Temporal changes of the land surface temperature due to land cover modifications within the last decades were detected based on day-time images of 1989, 2003 and 2018. Hereby, urbanization/industrialization (e.g. Jurong Island, see Fig. 5), as well as deforestation (e.g. Johor Bahru) and land reclamation (e.g. Changi Airport, see Fig. 6) were the main sources for an increase of the land surface temperature over time:
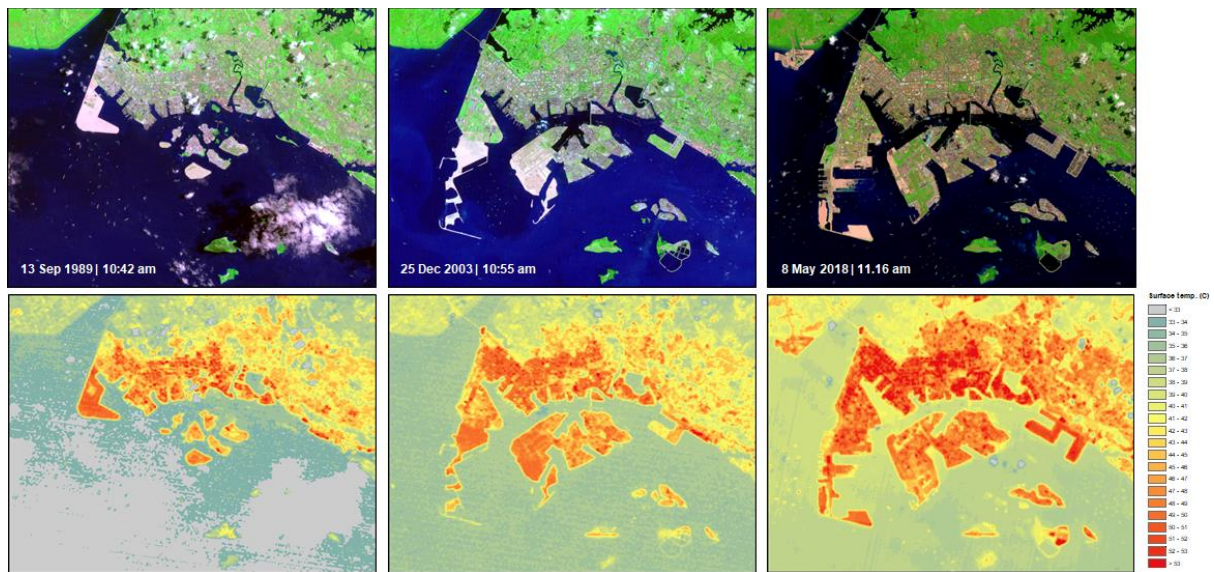
Figure 5. Land use changes and related surface temperatures of Jurong Island (1989, 2003 and 2018) (Source: Earthexplorer 2019).
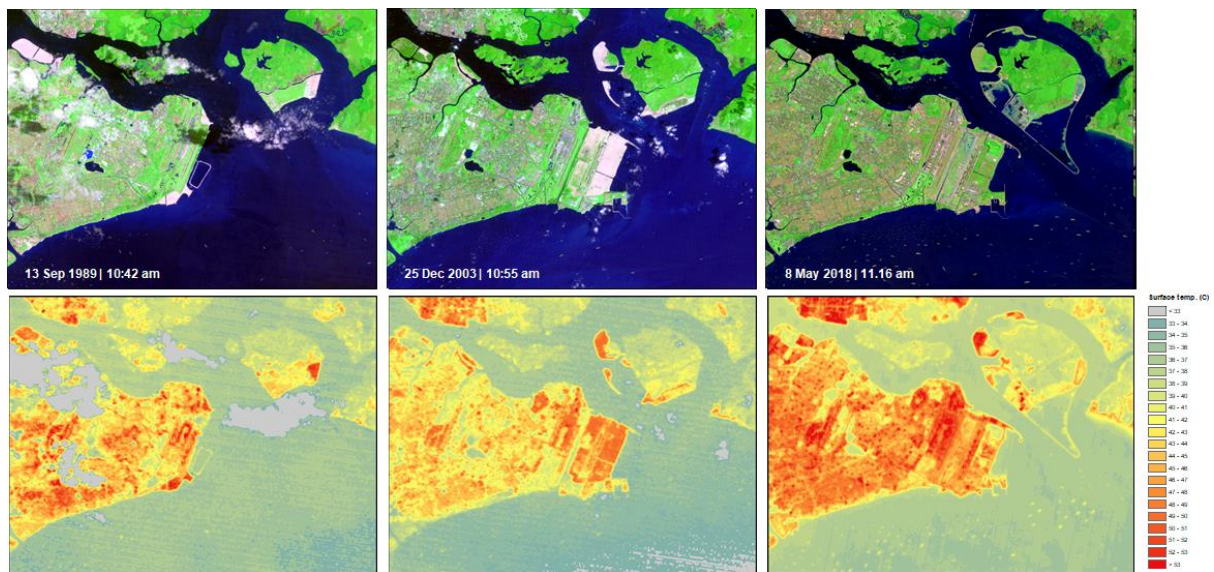
Figure 6. Land use changes and related surface temperatures of Changi Airport (1989, 2003 and 2018) (Source: Earthexplorer 2019).

- The Local Climate Zones (LCZ) considered as urban are during day-time the warmest areas of Singapore, whereby the LCZ considered as rural are the colder areas within Singapore (see Figs. 7 and 8). The average temperature difference between urban LCZs and the rural vegetation related LCZs is within the day-time of 24 May 2018 about 6 degrees. Water is about 2 degrees Celsius colder than vegetation and thus the coldest land cover type.
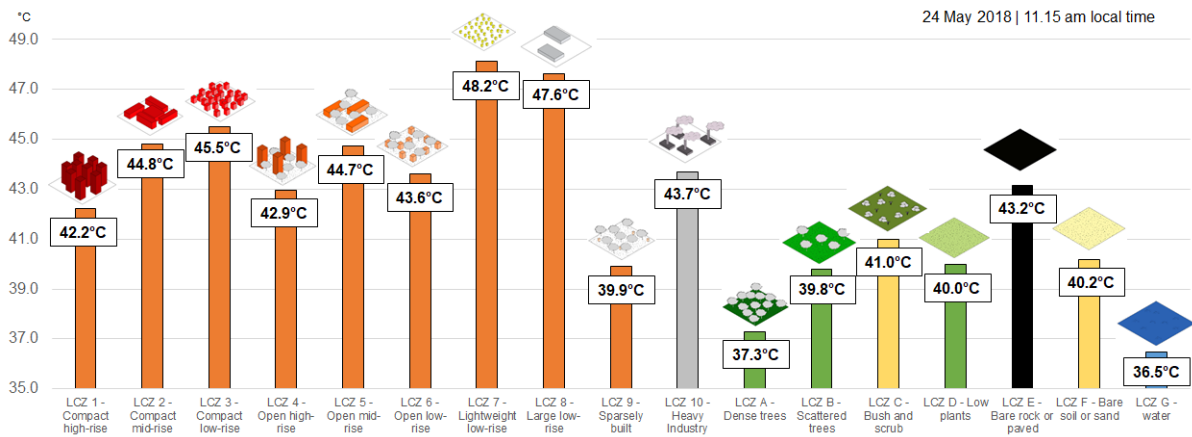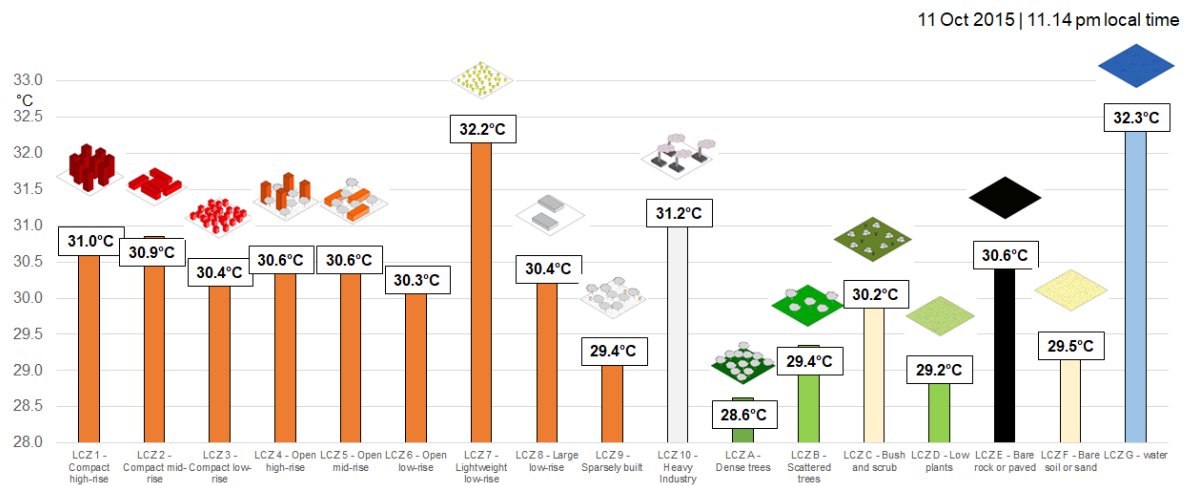
Figure 7. Average surface temperature for the LCZ during day-time (24 May 2018, 11.15am) (Source: Earthexplorer 2019, Mughal et al., 2019).
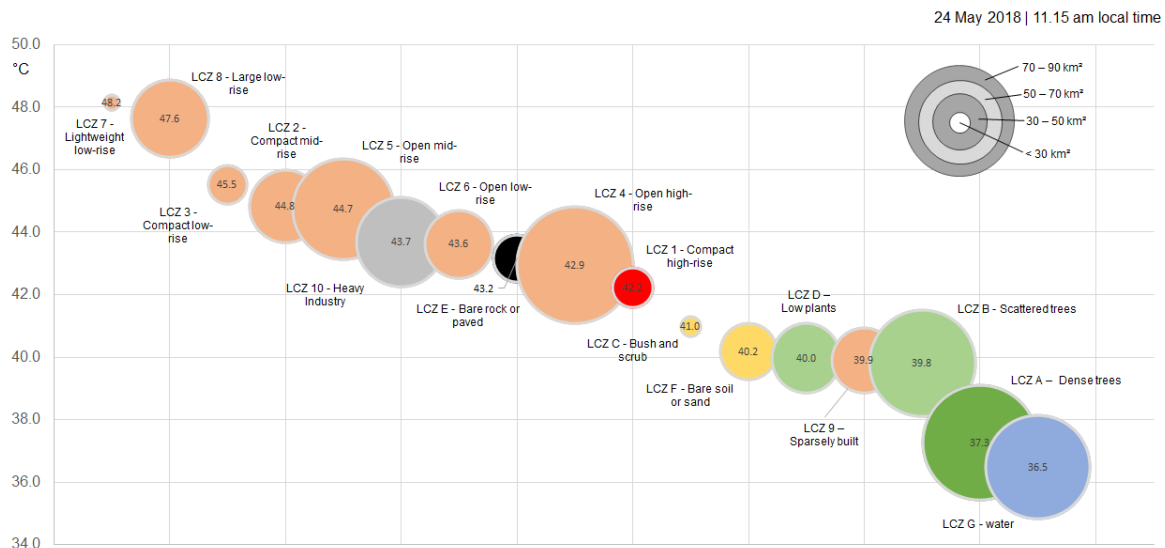
Figure 8: Weighted average surface temperature for the LCZ during day-time (24 May 2018, 11.15am) (Source: Earthexplorer 2019, Mughal et al., 2019).

- The LCZs considered as urban are during night-time the warmest areas of Singapore, whereby the LCZs considered as rural are, except for water through its thermal capacity, the colder areas within Singapore (see Fig. 9 and 10). The average temperature difference between urban LCZs and the rural vegetation related LCZs is within the night-time of 11 October 2015 (2 degrees), with LCZ water having the highest temperature due to its heat capacity.

Figure 9. Average surface temperature for the LCZ during night-time (11 October 2015, 11.14pm) (Source: Earthexplorer 2019, Mughal et al., 2019).
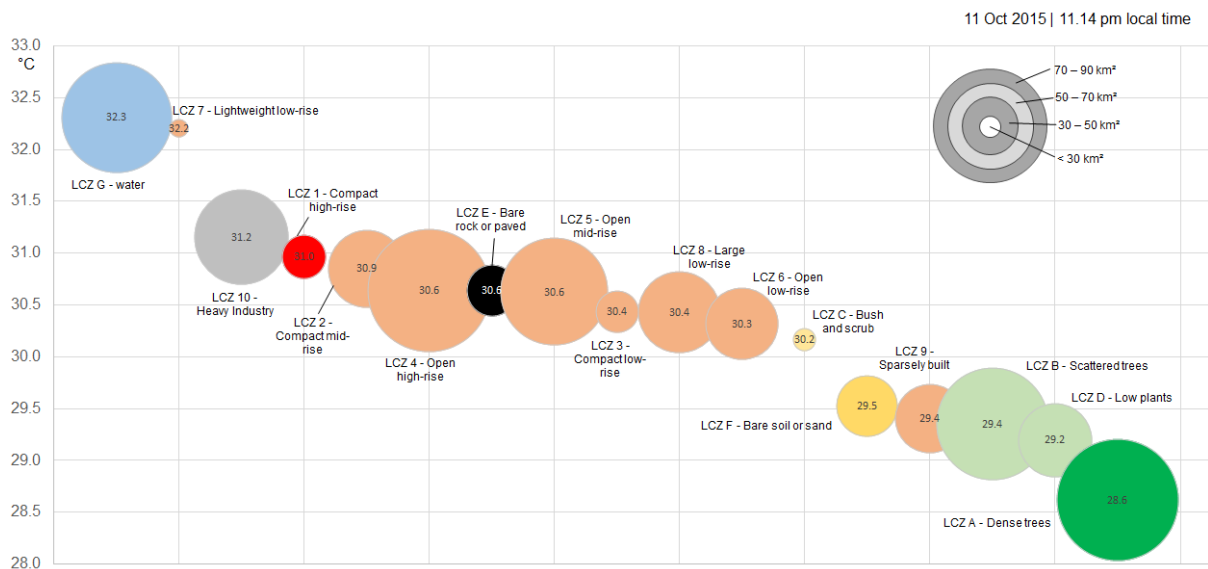

Figure 10. Weighted average surface temperature for the LCZ during night-time (11 October 2015, 11.14pm) (Source: Earthexplorer 2019, Mughal et al., 2019).

- The surface temperature of the hot spots (5% hottest areas) within the day-time images of 2018 in relation to LCZ could be detected (Fig. 11). Large low-rise buildings, heavy industry and open-mid-rise contain 78.9% of the hot spot areas in the day image.
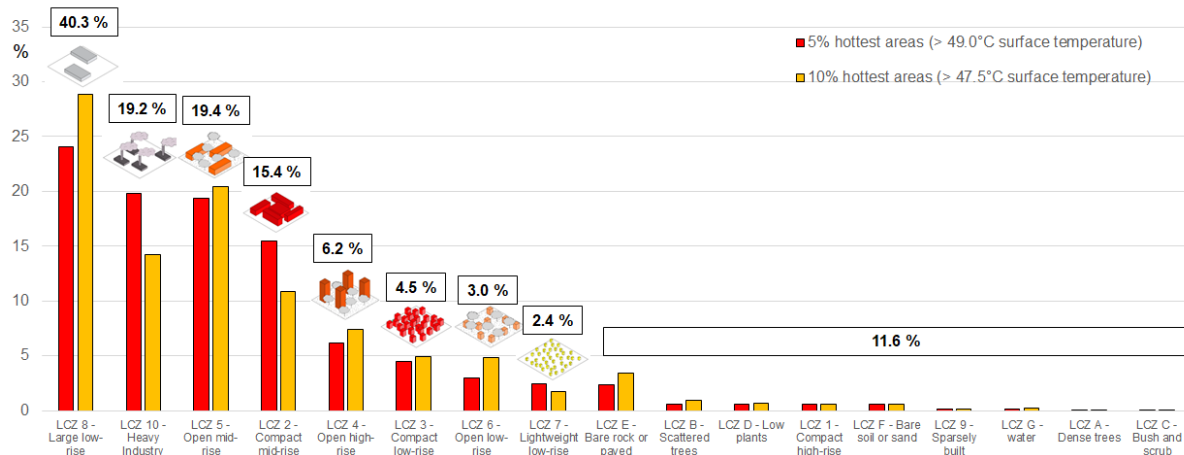
Figure 11. Highest surface temperature versus Local Climate Zones during day-time (24 May 2018, 11.15am) (Source: Earthexplorer 2019, Mughal et al., 2019).

- The surface temperature of the cold spots (5% coldest areas) during day-time in relation to LCZ could be detected (see Fig. 12). Dense trees and water contain 81.2% of the cold spots in the day image.
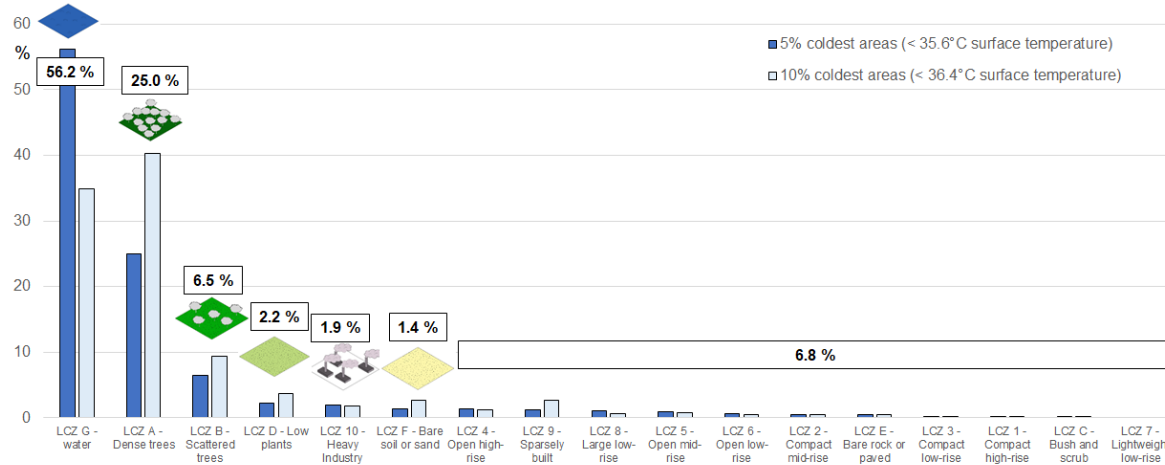
Figure 12. Lowest surface temperature versus Local Climate Zones during day-time (24 May 2018, 11.15am) (Source: Earthexplorer 2019, Mughal et al., 2019).

- The surface temperature of hot spots (5% hottest areas) within the night-time image from 11 October 2015 in relation to LCZ could be detected (see Figure 13). Water contains, through its heat capacity, more than 60% of the hot-spot areas, followed by 15% of heavy industry related areas in the night image.
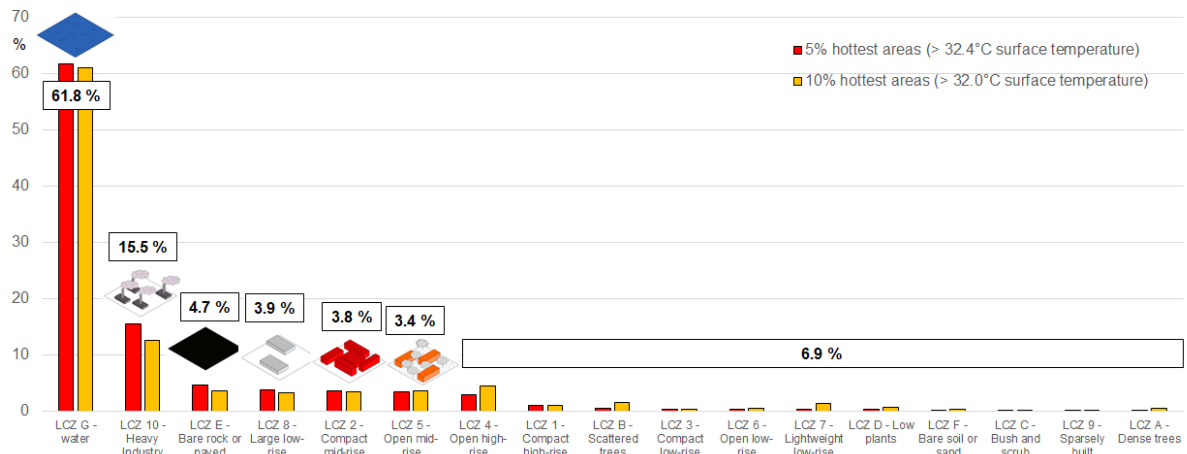
Figure 13. Highest surface temperature versus Local Climate Zones during night-time (11 October 2015, 11.14pm) (Source: Earthexplorer 2019, Mughal et al., 2019).

- The surface temperature cold spots (5% coldest areas) during the night-time image of 11 October 2015 in relation to LCZ could be detected (see Fig.14). Dense trees and scattered trees contain 60% of the cold spots in the night image.
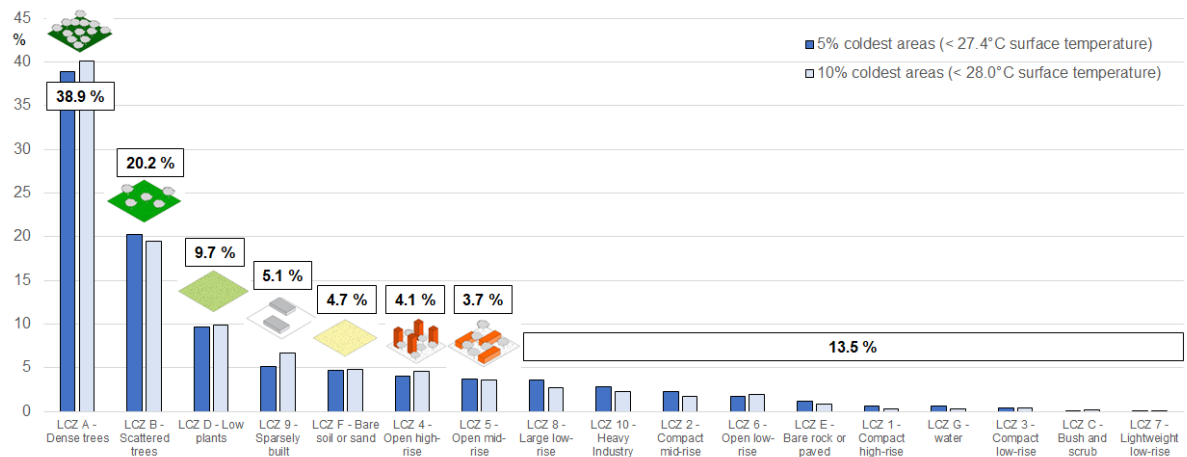
Figure 14. Lowest surface temperature versus Local Climate Zones during night-time (11 October 2015, 11.14pm) (Source: Earthexplorer 2019, Mughal et al., 2019).

- It was possible to locate the hottest and coldest plan areas by means of satellite imageries of 2018, 11.15am and 2015, 11.14pm (see Fig. 15 and 16).
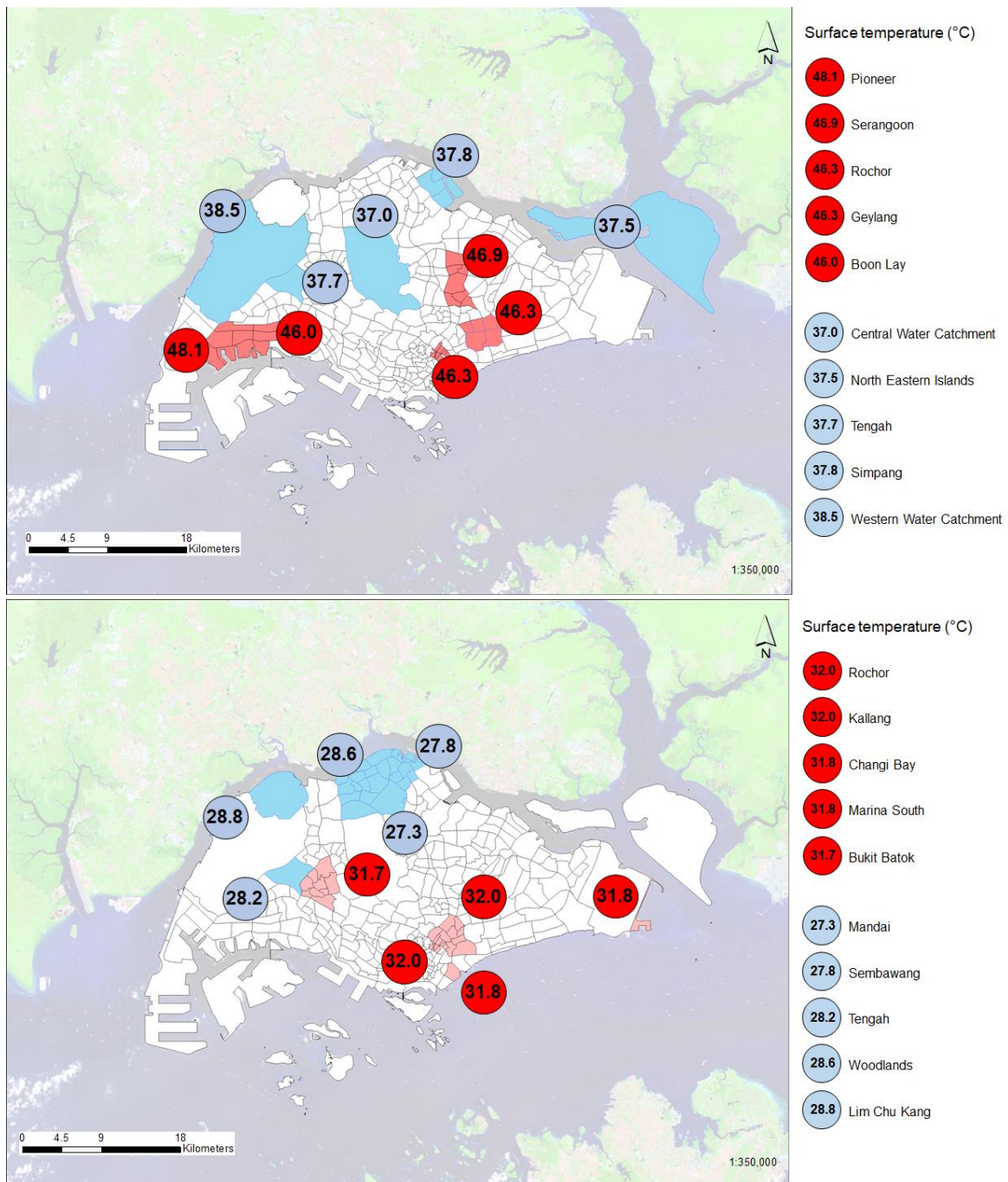
Figure 15 and 16: Surface temperatures of the five hottest and five coldest plan areas for the day image 2018 (above) and night image 2015 (below) (Source: Earthexplorer 2019, DATA-GOV 2019).

- The remote sensing data could be post-processed for visualising purposes in Singapore Views (see Figure 17).
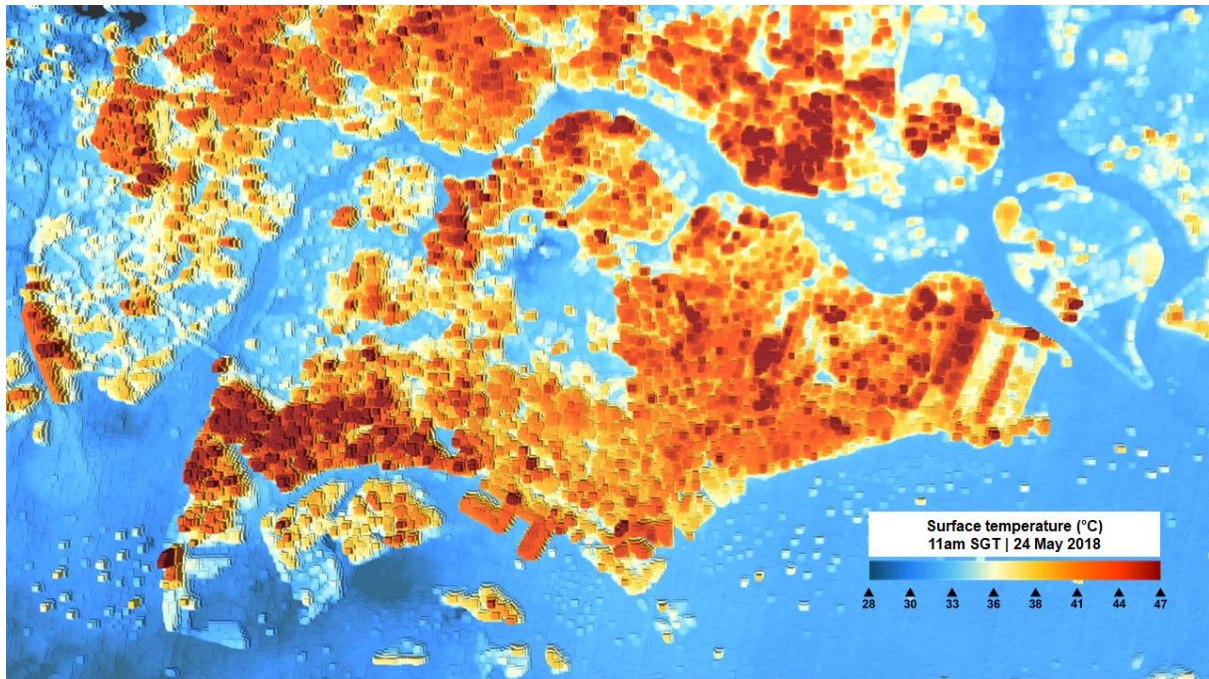
Figure 17. Visualization of remote sensing surface temperature data of 24 May 2018 in Singapore Views (Source: Earthexploerer 2019, Sailin Zhong, Conrad Philipp, Wang Ran, Mughal et al., 2019 and CIVAL at Future Cities Lab,).

- Environmental input data, products and information that shape the exposure to urban heat, such as land cover, street geometry, building volume, large floor area, aspect ratio, shading, land use and land surface, could be provided to be directly integrated into climate models (e.g. SingV, WRF).

- Data about the surface temperature could be generated that help to support the validation of the meso-scale canopy-layer models (e.g. SingV, WRF).

5 Conclusions

5.1 Summary of findings

- It was feasible to calculate the surface temperature for Singapore via satellite based remote sensing data, under the challenging circumstance of frequent cloud coverage above Singapore, and to map temporal changes of the Surface Urban Heat Island (S-UHI) over the last decades.
- Environmental input data, products and information that shape the exposure to urban heat, such as land cover, street geometry, building volume, large floor area, aspect ratio, shading, land use and land surface, to be directly integrated into climate models (e.g. SingV, WRF) could be provided.
- It was practicable to provide data that help to support the validation of the meso-scale canopy-layer models (e.g. SingV, WRF)
- It was possible to investigate the temporal changes of S-UHI due to land cover modifications from day-time images of 1989, 2003 and 2018.
- It was feasible to compare the Land Surface Temperature (LST) vs Local Climate Zones (LCZ) based on a 2018 day-time image and a 2015 night-time image.
- It was possible to locate the hottest and coldest districts (based on LST) with the help of satellite images of 2018, 11.15am and 2015, 11.14pm.
- It was feasible to locate the hot and cold spots in relation to LCZ (based on LST) using satellite imageries of 2018, 11.15am and 2015, 11.14pm.
- The generated data will be able to support the guidance on Urban Planning / Urban Geometry to mitigate UHI and optimize Outdoor Thermal Comfort (OTC).
- The remote sensing data will support the development of a Vulnerability Map.
- The generated remote sensing data will support the comparison of surface-UHI and air temperature-UHI (initially for CS1.5 and in-depth under CS2.0).
- The calculated remote sensing data could be processed for Singapore Views for visualization purposes.
- Primary investigation of the surface temperature for Singapore will increase the interest in remote sensing for UHI examinations.

5.2 Limitations

- Availability of cloud-free images at adequate temporal resolution for respected areas of interest.
- Demand on high-resolution remote sensing imageries can lead to costs of up to SGD 100k.

6   References

Angel, S. et al. (2016). Atlas of urban expansion. Volume 1. New York: New York University Urban Expansion Program; United Nations Programme for Human Settlements; Lincoln Institute of Land Policy.

Barsi, J.A. et al. (2014). Landsat-8 Thermal 650 Infrared Sensor (TIRS) Vicarious Radiometric Calibration, Remote Sens. 2014, 6, 11607-11626.

Bechtel, B. & C. Daneke (2012). Classification of local climate zones based on multiple earth observation data, IEEE Journal of Selected Topics in Applied Earth Observations and Remote Sensing, IEEE, 5(4), 1191-1202.

Bechtel, B. et al. (2015). Mapping local climate zones for a worldwide database of the form and function of cities, ISPRS International Journal of Geo-Information. Multidisciplinary Digital Publishing Institute, 4(1), 199-219.

Bechtel, B. et al. (2019). 'Generating WUDAPT Level 0 data–Current status of production and evaluation', Urban Climate, Elsevier, 27, 24-45.

Ching, J. et al. (2018). World urban database and access portal tools (WUDAPT), an urban weather, climate and environmental modeling infrastructure for the anthropocene, Bulletin of the American Meteorological Society.

Conrad, O. et al. (2015). System for automated geoscientific analyses (SAGA) v. 2.1. 4, Geoscientific Model Development, Copernicus GmbH, 8(7), 1991-1992.

Cui, Y.P. et al. (2016). Influence of urbanization factors on surface urban heat island intensity: a comparison of countries at different develop-mental phases, Sustainability 8, 706.

DATA-GOV (2019) <https://data.gov.sg/dataset/master-plan-2014-subzone-boundary-no-sea>, access on 12 July 2019

Earthexplorer 2019 <https://earthexplorer.usgs.gov>, access on 11 June 2019

Middel, A. et al. (2018). Sky view factor footprints for urban climate modeling, Urban Climate.

Mills, G. et al. (2015). An Introduction to the WUDAPT project, in Proceedings of the 9th International Conference on Urban Climate, Toulouse, France, 20-24.

Mughal, M. O., Li, X.-X., Yin, T.,Martilli, A., Brousse, O., Dissegna, M.A., & Norford, L. K. (2019). High-resolution, multilayer modeling of Singapore's urban climate in corporating local climate zones, Journal of Geophysical Research.

Peel M. C. et al. (2007). Updated world map of the Köppen-Geiger climate classification. Hydrology and Earth System Sciences Discussions, European Geosciences Union, 11, 5, 1633-1644.

Qin, Z.-H. et al. (2001). A mono-window algorithm for retrieving land surface temperature from Landsat TM data and its application to the Israel-Egypt border region. Int. J. Remote Sens. 2001, 22, 3719-3746.

Qiu, S. et al. (2017). Improving Fmask cloud and cloud shadow detection in mountainous area for Landsats 4–8 images, Remote Sensing of Environment. Elsevier, 199, 107-119.

Roth, M. (2013). 'Urban Heat Islands' in Handbook of Environmental Fluid Dynamics, Volume Two, ed. HJS Fernando, CRC Press/Taylor & Francis Group, LLC, 143-159.

Sobrino, J. A. et al. (1990). Significance of the remotely sensed thermal infrared measurements obtained over a citrus orchard, ISPRS J. Photogramm. Remote Sens., 44, 345-354.

Wang, C. et al. (2018). Assessing local climate zones in arid cities: The case of Phoenix, Arizona and Las Vegas, Nevada, ISPRS J. Photogramm. Remote Sens., 141, 59-71.

Wang, Z. et al. (2003). Nonlinear filtering for state delayed systems with Markovian switching. Ieee transactions on signal processing, 51, 9.

Wyoming 2019 <http://weather.uwyo.edu/upperair/sounding.html>, access on 14 June 2019

Zhu, Z. et al. (2015). Improvement and expansion of the Fmask algorithm: Cloud, cloud shadow, and snow detection for Landsats 4–7, 8, and Sentinel 2 images, Remote Sensing of Environment. Elsevier, 159, 269-277.

7 Links to other tasks under CS1.5 / CS2.0

- **Micro-scale / Mesoscale assessment (WRF)**
  Provide urban land cover, land use maps, surface temperature information and support the validation of the model.

- **Transport assessment**
  Derive fine-scale urban land cover and land use maps which can be fed into the traffic simulation model in order to quantify emissions from the current transport system.

- **Energy assessment**
  Provide a large variety of data sets, maps, statistics and insights to support the modelling of anthropogenic heat (e.g. night-time light images that can be correlated with anthropogenic heat emissions) to better understand the drivers of anthropogenic heat, particularly in Jurong Island.

- **Urban design assessment**
  Provide detailed information of high spatial and temporal resolution on the current state of urban environmental parameters, like land cover, street geometry, building volume, gross floor area, aspect ratio, shading, land use and land surface temperature.
  These layers can be used for comparison with future urban planning scenarios, climate-responsive urban layout variants and alternative/optimal urban designs identified by the semi-automated machine learning tools. Furthermore, they can be integrated into the stakeholder negotiation tool to form a baseline/reference scenario.

- **List of strategies**
  Support assessment on the current role of existing vegetation (trees, shrubs, grass), as well as, water bodies and their configuration in affecting outdoor thermal comfort.

- **Strategy validation**
  Produce city-wide maps of vegetation indicators and parameters at a spatial resolution of 20m. They will thus support the planned field surveys and manipulations conducted in different thermal environments and will help to upscale obtained experimental results.

- **Vulnerability map**
  Provide environmental data, products and information that shape the exposure to urban heat and include multi-sensor, long-term time series of land surface temperature and high spatial resolution layers of Singapore's urban environment (e.g. urban land cover/ use, fractional building, vegetation and water cover, 3D city model).

- **OTC range calibration**
  Provide urban land cover/land use maps and surface temperature information to support the validation of the model.

- **Cognitive study / Physiological study**
  Through a long-term analysis of land surface temperatures, remote sensing allows to reveal and characterize typical temperature hot spots. This information as a basis to identify suitable locations (i.e. with prolonged heat exposure), to identify locations featuring levels of heat exposure, identify regions of exceptional heat stress in Singapore, i.e., regions that particularly impact vulnerable people.

- **Willingness to pay / Cost-benefit analysis**
  Support analysing the environmental impact and effectiveness of different measures to mitigate Singapore's UHI. In this way, economic benefits of certain measures or their impacts on real estate prices can be better compared to their positive and/or negative environmental consequences.

- **Integration of models**
  The remote sensing data and products can either be directly integrated into climate models, or they can be compared with modelling results.

- **Climate Design Guidelines / Decision support system**
  Detailed planning and design guidelines to mitigate UHI and improve OTC will be supported by GIS analyses that can be implemented with the various remote sensing data/products and modelling results (time series of land surface temperature to identifying hot and cool spots on the island, deriving various maps on urban green and land surface temperature, which can be jointly investigated and integrated into models).

- **Data visualization**
  Remote sensing related data (e.g. surface temperature map for Singapore) will be visualized in Singapore Views.